Reducing the ionospheric contamination effects on the column O/N2 ratio and its application to the identification of non-migrating tides

Christopher Scott Krier[1], Scott L England[1], Robert R. Meier[2], and Harald U. Frey[3]

[1]Virginia Polytechnic Institute and State University
[2]George Mason University
[3]University of California, Berkeley

December 7, 2022

Abstract

Prior investigations have attempted to characterize the longitudinal variability of the column number density ratio of atomic oxygen to molecular nitrogen (ΣO/N2) in the context of non-migrating tides. The retrieval of thermospheric ΣO/N2 from far ultra-violet (FUV) emissions assumes production is due to photoelectron impact excitation on O and N2. Consequently, efforts to characterize the tidal variability in O/N2 have been limited by ionospheric contamination from O+ radiative recombination at afternoon local times (LT) around the equatorial ionization anomaly. The retrieval of ΣO/N2 from FUV observations by the Ionospheric Connection Explorer (ICON) provides an opportunity to address this limitation. In this work, we derive modified ΣO/N2 datasets to delineate the response of thermospheric composition to non-migrating tides as a function of LT in the absence of ionospheric contamination. We assess estimates of the ionospheric contribution to 135.6 nm emission intensities based on either Global Ionospheric Specification (GIS) electron density, International Reference Ionosphere (IRI) model output, or observations from the Extreme Ultra-Violet imager (EUV) onboard ICON during March and September equinox conditions in 2020. Our approach accounts for any biases between the ionospheric and airglow datasets. We found that the ICON-FUV dataset, corrected for ionospheric contamination based on GIS, uncovered a previously obscured diurnal eastward wavenumber 2 tide in a longitudinal wavenumber 3 pattern at March equinox in 2020. This finding demonstrates not only the necessity of correcting for ionospheric contamination of the FUV signals but also the utility of using GIS for the correction.

Hosted file

`essoar.10512866.1.docx` available at https://authorea.com/users/557195/articles/611055-reducing-the-ionospheric-contamination-effects-on-the-column-o-n2-ratio-and-its-application-to-the-identification-of-non-migrating-tides

Hosted file

`supporting_information.docx` available at https://authorea.com/users/557195/articles/611055-reducing-the-ionospheric-contamination-effects-on-the-column-o-n2-ratio-and-its-application-to-the-identification-of-non-migrating-tides

Reducing the ionospheric contamination effects on the column O/N_2 ratio and its application to the identification of non-migrating tides

Christopher S. Krier[1], Scott L. England[1], R. R. Meier[2,3], and Harald U. Frey[4]

[1]Aerospace and Ocean Engineering, Virginia Polytechnic Institute and State University, Blacksburg, VA, USA

[2]Department of Physics and Astronomy, George Mason University, Fairfax, VA, USA

[3]Naval Research Laboratory, Emeritus, Washington, DC, USA

[4]Space Sciences Laboratory, University of California Berkeley, Berkeley, CA, USA

Corresponding author: Christopher S. Krier (`ckrier@vt.edu`), ORCID: 0000-0002-3786-4094

Key Points:

1. The ionospheric contribution to daytime emissions at 135.6 nm observed by ICON-FUV is estimated using either GIS, IRI, or ICON-EUV data

2. To characterize non-migrating tides in column O/N_2, we generate modified datasets in which ionospheric contamination effects are reduced

3. Contrary to the unmodified dataset, the modified dataset generated using GIS data indicates the DE2 tide during March-April 2020

Abstract

Prior investigations have attempted to characterize the longitudinal variability of the column number density ratio of atomic oxygen to molecular nitrogen ($\Sigma O/N_2$) in the context of non-migrating tides. The retrieval of thermospheric $\Sigma O/N_2$ from far ultra-violet (FUV) emissions assumes production is due to photoelectron impact excitation on O and N_2. Consequently, efforts to characterize the tidal variability in $\Sigma O/N_2$ have been limited by ionospheric contamination from $O^+ + e$ radiative recombination at afternoon local times (LT) around the equatorial ionization anomaly. The retrieval of $\Sigma O/N_2$ from FUV observations by the Ionospheric Connection Explorer (ICON) provides an opportunity to address this limitation. In this work, we derive modified $\Sigma O/N_2$ datasets to delineate the response of thermospheric composition to non-migrating tides as a function of LT in the absence of ionospheric contamination. We assess estimates of the ionospheric contribution to 135.6 nm emission intensities based on either Global Ionospheric Specification (GIS) electron density, International Reference Ionosphere (IRI) model output, or observations from the Extreme Ultra-Violet imager (EUV) onboard ICON during March and September equinox conditions in 2020. Our approach accounts for any biases between the ionospheric and airglow datasets. We found that the ICON-FUV dataset, corrected for ionospheric contamination based on GIS, uncovered a previously obscured diurnal eastward wavenumber 2 tide in a longitudinal wavenumber 3 pattern at March

1

equinox in 2020. This finding demonstrates not only the necessity of correcting for ionospheric contamination of the FUV signals but also the utility of using GIS for the correction.

1) Introduction

The propagation and dissipation of large-scale atmospheric waves play an important role in the dynamics of the thermosphere. Solar thermal atmospheric tides are planetary-scale waves (primarily driven by the absorption of solar radiation) with periods that are subharmonics of a solar day. Non-migrating tides do not follow the apparent motion of the Sun across the sky and some of the most important tidal components have been shown to originate from the lower atmosphere via large-scale tropospheric latent heat release and the differences in absorption of solar radiation caused by the land-sea distribution (Forbes et al., 2006; Hagan and Forbes, 2002). The longitudinal/local time modulation of the mesosphere/lower thermosphere (MLT) winds (Liebermann et al., 2013), neutral temperature (Forbes et al., 2008), and the composition of minor constituents (Oberheide et al., 2013) have been observed to correlate with the signatures of non-migrating tides. Additionally, the tidal impact on the ionosphere has been well documented in observations (Immel et al., 2006; Sagawa et al., 2005) and has been confirmed by model simulations (Chang et al., 2013, Goncharenko et al., 2010; Pedatella et al., 2011).

The tidal nomenclature used in this paper is standard in the literature. DE3, for example, is the diurnal tide (24 hour period) that is eastward propagating with zonal wavenumber 3 at a fixed universal time. Likewise, SW1 is the semidiurnal tide (12 hour period) that is westward propagating with zonal wavenumber 1 at a fixed universal time. A tide with period, in cycles per day, n and zonal wavenumber s (where $s < 0$ indicates eastward propagation) causes a longitudinal wavenumber $|n - s|$ in a reference frame relative to a fixed local solar time (Forbes et al., 2008).

The column number density ratio of atomic oxygen to molecular nitrogen, referred to as $\Sigma O/N_2$, is a diagnostic of thermospheric composition first proposed by Strickland et al. (1995) and Evans et al. (1995) as a means of retrieving atmospheric composition information from measurements of the ratio of photoelectron-excited OI 135.6 nm / N_2 LBH bands in the far ultra-violet (FUV). It has been hypothesized that non-migrating tides substantially impact the $\Sigma O/N_2$ ratio. Atmospheric theory predicts that tides perturb $\Sigma O/N_2$ as a result of the species-dependent impact of the vertical tidal winds (Cui et al., 2014; England et al., 2021). Indeed, these fluctuations appear in physics-based models of the thermosphere (England et al., 2010; Jones et al., 2014; Roble and Shepherd, 1997). Variations in $\Sigma O/N_2$ can also modify the photochemical equilibrium of the thermosphere and thus the associated F-region ionospheric density (Lean et al., 2011; England, 2012). Model results suggest that $\Sigma O/N_2$ variations contribute at least ~30% of the total variation in ionospheric density (England et al., 2010). To obtain a complete picture of tidal-ionosphere coupling, it is important that the tidal modification of $\Sigma O/N_2$ be well-understood.

Previous attempts to characterize the tidal perturbations in $\Sigma O/N_2$ focused on retrievals from FUV emissions observed by the Global Ultraviolet Imager (GUVI) onboard the Thermosphere, Ionosphere, Mesosphere Energetics and Dynamics (TIMED) satellite which provided limb observations of $\Sigma O/N_2$ from 2002-2007 and on the disk from 2002-present (Christensen et al., 2003; Meier et al., 2015). Zhang et al., (2010) found wave-4 and wave-3 perturbations on the order of 10% of the background GUVI $\Sigma O/N_2$ during the boreal fall and summer seasons respectively, hypothesizing that these can be explained by the influence of the DE3 and DE2 non-migrating tides. Model simulations of England et al., (2010) indicate that a 10% perturbation of $\Sigma O/N_2$, translates to about a 1/3 contribution to the connected ionospheric F-region density variations. A comprehensive analysis of the wavenumber structure found in GUVI $\Sigma O/N_2$ was presented by He et al. (2010). Based on GUVI data from 2002–2007, they confirmed that the seasonal variation of the wavenumber-4 structure is consistent with that of the strength of the DE3 tide, but the evolution as a function of local time was found to be stationary instead of eastward as would be expected by modulation caused by DE3.

In addition to those produced by the excitation of the ground state atomic oxygen by the impact of photoelectrons and subsequent deexcitation, OI 135.6 nm emissions can also be produced by $O^+ + e$ radiative recombination (RR) in the F-region of the ionosphere (Meier, 1991). Consequently $\Sigma O/N_2$ retrievals from the thermospheric dayglow can be compromised because large O^+ densities can occur at afternoon local solar times around the equatorial ionization anomaly. Work has been done to demonstrate the impact of the ionospheric contamination on the identification of tides in $\Sigma O/N_2$. With GUVI limb radiance profiles, Kil et al., (2011) showed that the longitudinal variations in GUVI $\Sigma O/N_2$ are mainly a consequence of the ionospheric contamination. Kil et al., (2013) subsequently quantified the impact of the ionosphere on the GUVI $\Sigma O/N_2$, estimating the contribution to be about 10%. Recently, Zhang et al., (2021) presented a new algorithm that separates the thermospheric and ionospheric contributions to the GUVI radiances at 135.6 nm and they show results of clean $\Sigma O/N_2$ that are consistent with $\Sigma O/N_2$ as a purely thermospheric quantity. The approach proposed by Zhang et al. (2021) takes advantage of the emission at 130.4 nm observed by GUVI. Using $\Sigma O/N_2$ from the Global-Scale Observations of the Limb and Disk (GOLD), Krier et al., (2021) showed observations of non-migrating diurnal tides in GOLD $\Sigma O/N_2$ based on dusk – dawn differences and included a discussion of potential ionospheric contamination effect, concluding that the impact could vary by season with the higher impact during boreal fall than that during boreal winter.

Observations of the $\Sigma O/N_2$ ratio from the Far Ultra-violet Imager (FUV) onboard the Ionospheric Connection Explorer (ICON; Immel et al., 2017) provide an opportunity to study non-migrating tides in thermospheric composition (England et al., 2021). The rapid local time precession afforded by the ICON observatory in a 27° inclined orbit is a distinct advantage because seasonal variations do not strongly alias into the tidal signal during the time required to sample all

local solar times (~27 days) . As indicated by the previous investigations discussed above, the effects of ionospheric contamination must be considered in any tidal analysis of $\Sigma O/N_2$. Since ICON-FUV does not observe emissions at 130.4 nm, the approach proposed by Zhang et al., (2021) is not feasible for ICON. As an alternative approach, we calculate the ionospheric contribution based on a variety of datasets including Global Ionospheric Specification (GIS), the International Reference Ionosphere, and the Extreme Ultraviolet (EUV) instrument on ICON.

The objectives of this study are the following:

(1) Calculate the ionospheric contribution to the ICON-FUV observations at 135.6 nm along the line of sight of $\Sigma O/N_2$ retrieval based on three different data sources: GIS, the International Reference Ionosphere (IRI), and the ICON EUV Imager. To scale the calculations such that biases of the datasets are minimized, we leverage nighttime ICON-FUV observations in which only the ionospheric contribution is present.

(2) Derive modified ICON-FUV $\Sigma O/N_2$ datasets which have been corrected for ionospheric contamination.

(3) Delineate the response of $\Sigma O/N_2$ to non-migrating tides as a function of local time and compare amplitudes to those of modeled tides from the TIEGCM (Thermosphere Ionosphere Electrodynamics General Circulation Model). Importantly, identify any changes in the non-migrating tidal structure seen in the original and modified datasets.

This paper is organized as follows. Section 2 describes the data and models used in the present work. Section 3 presents our methodology. Section 4 shows the relevance of the analyses to the three objectives. Section 5 puts Section 4 into context using physics based models. Section 6 contains a summary and closing remarks.

2) Data and Models

2.1 ICON Far-Ultraviolet Observations

The ICON Far-Ultraviolet Imager (ICON-FUV) is a spectrographic imager that observes airglow emissions in two separate wavelength passbands: short wave (SW) centered on the OI doublet at 135.6 nm and long wave (LW) including a portion of the Lyman-Birge-Hopfield (LBH) bands centered on 157 nm (Mende et al., 2017). Images of the airglow capture both the Earth's limb up to about 500 km tangent altitude and downward onto the disk to an angle about 58° from nadir. ICON-FUV points perpendicular to the spacecraft velocity vector such that during normal observational conditions, ICON-FUV points true north at the transition between ascending and descending orbit nodes. The thermospheric $\Sigma O/N_2$ is inferred from the ratio of the daytime column brightness intensity ratio of SW to LW on the disk of the Earth about 7.5° great circle away from the ICON observatory (Meier, 2021; Stephan et al., 2018). During

conditions of atmospheric darkness, ICON-FUV observes the O^+ + e radiative recombination emission in the SW channel from which O^+ density profiles are derived (Kamalabadi et al., 2017). Wautelet et al. (2021) compared the retrieved nighttime O^+ density profiles to ground-based and COSMIC-2 data sets and found ~50% positive bias in the ICON-FUV values based on calibrated radiances in Version 3 of the FUV database.

Each image of calibrated column brightness is separated into 6 vertical stripes each constituting a vertical profile integrating 3° of horizontal field of view. The $\Sigma O/N_2$ disk inversion takes as input the average of 21 pixels on the disk in the stripe corresponding to 0° to 3° along the horizontal field of view (referred to as stripe P0 in ICON-FUV Level 1 data products, https://icon.ssl.berkeley.edu/Data/Data-Product-Matrix).

This work uses Version 4 of $\Sigma O/N_2$ data and Version 3 of the calibrated far-ultraviolet radiances, which were the latest available when this work was undertaken. In addition, this work reassesses part of the analysis of England et al. (2021) with the same $\Sigma O/N_2$ data version used therein. Because the focus of this paper is a method to remove the ionospheric contribution from the retrieval of $\Sigma O/N_2$ and its implications for the identification of upward propagating non-migrating tides, the actual version of radiances used is not of primary relevance; data version is accounted for with our calibration method (Section 3). Indeed, the recently released ICON-FUV Version 5 calibrated radiances report generally lower values, which turns out to be supported by this work (see Figure 2 and discussion in Section 3).

ICON flies in a 27° inclined orbit at about 590 km altitude. Figure 1 depicts the global distribution and local solar time sampling of one day of ICON-FUV $\Sigma O/N_2$ retrievals on August 22, 2020. The local solar time at any latitude is approximately fixed on any day and quickly moves to early local solar times as a function of day. The large gap in the southern hemisphere is due to the South Atlantic Anomaly where ICON-FUV is turned off. Therefore, we focus analysis on the northern hemisphere where full longitudinal sampling is afforded.
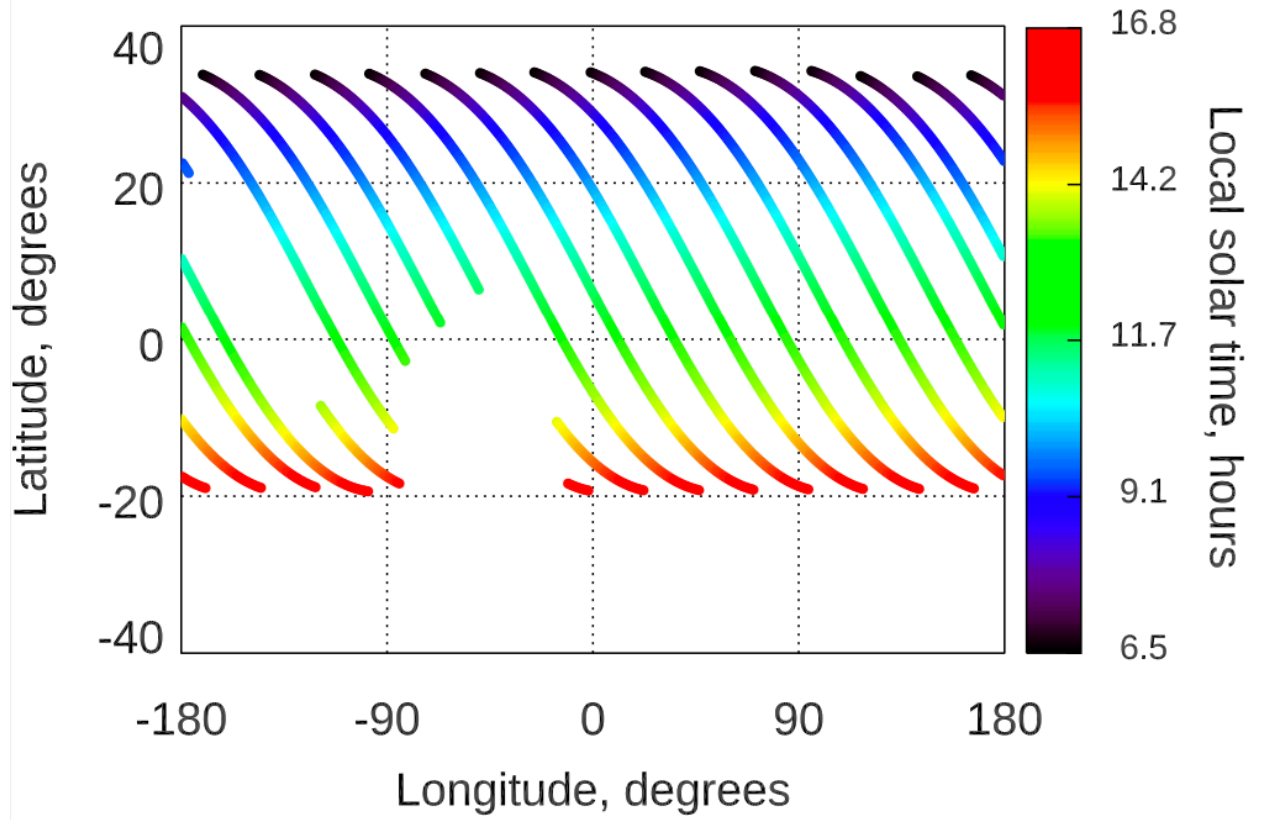
Figure 1. Global distribution and local time sampling of column disk O/N$_2$ observations on August 22, 2020 from the Far-Ultraviolet imager onboard the Ionospheric Connection Explorer. The gap in the southern hemisphere is due to the South Atlantic Anomaly. The gap between about 180° W and 120° E is due to a spacecraft maneuver.

2.2 Global Ionospheric Specification

GIS employs a data assimilative approach to produce hourly three-dimensional global maps of electron density (Lin *et al.*, 2017, 2020a). Radio occultations from COSMIC-2 and ground-based observations of slant Total Electron Content (TEC) are assimilated into the nowcast model using a Gauss-Markov Kalman filter algorithm in which the background is specified by the IRI. The IRI (Bilitza, 2001) is an empirical model that specifies various ionospheric parameters on a monthly basis, away from the auroral zone and during undisturbed conditions. IRI draws upon observations from various sources including ionosondes, incoherent coherent radar, and spacecraft. The latitude-longitude-altitude resolution of the GIS output is 2.5° by 5° by 20 km. Lin et al. (2020b) and Wang et al. (2021) employed GIS data to describe the planetary wave response of the iono-

sphere to Sudden Stratospheric Warmings. The GIS dataset has been shown to be useful in resolving the day-to-day tidal variability of the F-region ionosphere (Oberheide, 2022). These studies demonstrate the suitability of the GIS dataset for removal of the ionospheric effect on the identification of non-migrating tides in $\Sigma O/N_2$.

2.3 ICON-EUV O^+ Profiles

The ICON Extreme Ultraviolet spectrograph (ICON-EUV) is an imaging spectrometer that derives limb profiles of dayglow in a spectral range from 54 to 88 nm (Sirk et al., 2017). Altitude profiles of O^+ are inferred from the 61.7 nm O^+ triplet and the 83.4 nm O^+ triplet (Stephan et al., 2017). Here, we use Version 3 of the derived O^+ density profiles. ICON-EUV O^+ density profiles have been compared to observations from COSMIC-2, ground-based ionosondes, and incoherent scatter radar from 2019 to 2021. Wautelet et al. (2022) reported that EUV peak density (NmF2) is on the order 50-60% smaller than each of these datasets and that the differences in peak height HmF2 is consistent with the expected precision of the various data sources. Day-to-day variation in the bias of the EUV parameters are believed to be caused by effects due to ICON's orbital precession, precision of the calibrations, or limitations of the EUV inversion during prolonged and exceptional low solar activity. Nevertheless, ICON-EUV provides the spatial structure of the daytime ionospheric density required to remove global-scale ionospheric effects on the identification of non-migrating tides in $\Sigma O/N_2$. Since, the ICON-FUV disk and ICON-EUV limb sampling of a particular combination of local solar time and location is offset in time, our correction based on ICON-EUV O+ profiles (Section 3) is calculated using 45-day running means. Any mean potential offset in NmF2 is addressed by our methodology (Section 3).

2.4 Simulation of $\Sigma O/N_2$ by the TIEGCM-ICON

In Section 5 we refer to $\Sigma O/N_2$ modeled by the Thermosphere-Ionosphere-Electrodynamics General Circulation Model for the Ionospheric Connection Explorer (TIEGCM-ICON; Maute, 2017). In this version of the TIEGCM, the lower boundary at ~97 km is perturbed by atmospheric tides derived from the ICON-MIGHTI observations of horizontal winds (Harding et al., 2017) and temperature (Stevens et al., 2018) to simulate the thermospheric and ionospheric conditions in the real-time atmosphere experienced by ICON. The Hough Mode Extension (HME) technique (Cullens et al., 2020; Forbes et al., 2017) is applied to MIGHTI temperature and horizontal winds (~90-103 km altitude range) to self-consistently specify the global tidal spectrum in neutral winds and temperature throughout the thermosphere. We note that there are some limitations to this approach because of the asymmetrically incomplete latitudinal/longitudinal sampling afforded by ICON-MIGHTI. Since ICON-MIGHTI samples latitudes from 10° south–40° north and misses a large sector of longitudes in the southern hemisphere due to the SAA, tidal aliasing can lead to higher uncertainties in the tides (Cullens et al., 2020; Forbes et al., 2017). $\Sigma O/N_2$ is calculated relative to the standard N_2 column depth of 10^{17} molecule cm^{-2}, first specified by

Strickland et al. (1995); also see Meier (2021). In Section 5, we compare amplitudes derived from a full tidal decomposition of the model to those observed in ICON-FUV.

3) Removing Ionospheric Contamination from column O/N$_2$ retrieved by ICON-FUV

Since $\Sigma O/N_2$ is derived from the ratio of the shortwave (SW) channel to the longwave (LW) channel column emission rates, the effects of ionospheric contamination can be reduced in the retrieval of $\Sigma O/N_2$ by subtracting an estimate of the ionospheric contribution from the SW radiance. We estimate the ionospheric contribution by calculating path integrals from the ICON observatory to the reference remote point altitude at 150 km. The 135.6 nm emission of ionospheric origin can be modeled (Equation 1) as the sum of contributions from radiative recombination between electrons and oxygen ions (first term) and ion-ion mutual neutralization (second term).

$$I_{\mathrm{RR}} = \frac{1}{10^6} \int \alpha_{1356}\left(T_e\right) N_e \left[O^+\right] ds + \frac{\beta_{1356} k_1 k_2}{10^6} \int \frac{N_e[O][O^+]}{k_2 \left[O^+\right] + k_3[O]} ds \qquad (1)$$

Equation 1 ignores multiple scattering of 135.6 nm photons that is considered in the nighttime ionospheric retrievals (Kamalabadi et al., 2018). The radiative recombination term is the principal term (Meier, 1991). A description of the constants in Equation 1 is provided by Table 1. The line of sight from the spacecraft to the remote point is discretized into 50 segments for which a value for electron temperature T_e, electron density N_e, and atomic oxygen density [O] is calculated. We assume that $N_e = O^+$ at all altitudes above 150 km. NRLMSISE-00 (Picone et al., 2002) and IRI are used to specify [O] and T_e respectively. As stated earlier, we test three data sets for specification of the electron density term: GIS, the IRI, and the ICON EUV spectrometer. Electron density along the line of sight is determined using GIS and IRI output by using the nearest neighbor model grid point. For the modified dataset based on ICON-EUV, since ICON-EUV limb O^+ retrievals and ICON-FUV $\Sigma O/N_2$ retrievals are not sampled at the same local solar time and location for a given day, a sliding 45-day window climatology is used to determine N_e based on observed O^+ profiles. The average is taken of EUV O^+ limb profiles within the 45-day window whose tangent location is within 15 deg longitude, 0.5 deg latitude and 20 minutes local solar time of the line of sight location at 300 km. We leave out the following O^+ profiles from the average: (1) those with a reported EUV quality flag greater than 1 which correspond to retrievals not recommended for use in any analysis, (2) those with NmF2 greater than 4.8 $\times 10^6$ cm^{-3} , and (3) those with NmF2 greater than 3 standard deviations of the mean NmF2 during the 45-day window. The cutoff value of 4.8 $\times 10^6$ cm^{-3}, following the work of Chang et al. (2013), is based on long-term ionosonde observations by Liu et al. (2006) who found that NmF2 maximized at about 3×10^6 cm^{-3} for F10.7 cm index about equal to 300 sfu.

|		
α_{1356}	Radiative recombination rate	$7.3 \times 10^{-13} \times (1160/T_e)^{0.5}$
β_{1356}	Ion-ion neutralization yield	0.54
k_1	Radiative attachment	1.3×10^{-15}
k_2	Ion-ion neutralization rate	10^{-7}
k_3	Ion-atom neutralization rate	1.4×10^{-10}

Table 1. Summary of coefficients used in Equation (1). All values are based on the work of Meléndez-Alvira et al. (1999) and references therein.

The analysis presented in the following section uses Level 1 Version 3 ICON-FUV data products (calibrated radiances) which are now known to be too high by about 30% (Frey et al., 2022). To account for this and calibrate our calculations of the ionospheric contribution to the emission at 135.6 nm (Equation 1), we determine a scale factor which is applied to the modeled ionospheric emissions. The scale factor is determined by comparing our model to observed ICON-FUV shortwave limb radiances during nighttime, when the total emission is due to the ionosphere. Three weeks of data are used for each time period. The comparison is limited to data between $\pm15°$ magnetic latitude, between 21:00 and 24:00 LST, and at a solar zenith angle greater than 110°. The altitude resolution of the ICON-FUV limb profiles (~4 km) is degraded to match that of GIS output (20 km). The quantity for comparison is the average radiance between 20 and 40 km above the altitude of the peak. For this comparison, the path integral to calculate the total brightness along the line of sight extends past the reference disk retrieval location at 150 km altitude back to ICON's orbit altitude to account for the line of sight along the limb.

Figure 2 shows scatter plots comparing the observed ICON-FUV SW brightness against the modeled brightness based on the GIS ionosphere, from DOY 73-94 in 2020 at the sampling of magnetic latitude / LST and observing geometry discussed above. Figure 2a and 2b use Versions 3 and 5 FUV L1 data respectively. The equation for the line of best fit, scale factor (inverse of the slope) and its uncertainty, and linear correlation coefficient (R) are shown in each panel. Our analysis for Version 3 (Figure 2a) yields a scale factor equal to 4.02 ±0.17 . Thus, increasing our calculated brightness based on GIS by a factor of 4 normalizes our model to the relative sensitivity of the ICON-FUV instrument in Version 3 and allows us to properly treat for ionospheric contamination. Similarly, the scale factor for DOY 218-241 was determined to be ~3.5. These scale factors are consistent with the work of Wautelet et al. (2021) who found a mean positive difference of 55% between ICON-FUV and COSMIC-2 values for nighttime NmF2. Note that the ionospheric radiative recombination emission is proportional to the square of the ionospheric density (Equation 1). Figure 2a and 2b demonstrate that the scale factor is version dependent and this normalization process must be performed for each data version and dataset. The scale factor used to normalize the modeled ionospheric contribution based on IRI is assumed to be equal to that determined for GIS since IRI serves as

the background to the GIS data assimilation scheme.

ICON-EUV does not retrieve O^+ profiles at night, therefore a direct comparison to ICON-FUV as was done for GIS is not possible. However, the calculated values (Equation 1) based on ICON-EUV can be compared to those based on GIS. Consequently, we determine a scale factor to apply to the calculated value based on EUV to normalize to those based on GIS. The scale factor to apply to ICON-EUV to normalize to ICON-FUV is then the product of two scale factors. The EUV-to-GIS scale factor is determined by comparing the magnitude of the respective brightness intensities along the ICON-FUV $\Sigma O/N_2$ retrieval. Ordered pairs are formed consisting of GIS and EUV brightness intensities in increasing order in terms of magnitude. The scale factor is derived from the line of best fit of these ordered pairs. This approach is necessary, since the calculated GIS- and EUV-based brightness are uncorrelated and would not yield a linear trend in a point-to-point comparison. For the 73-94 time period, the GIS-EUV scale factor was determined to be ~6. Therefore, the EUV-FUV scale factor is ~24. The necessity to scale EUV in this manner is consistent with the findings of Wautelet et al. (2022) who found that EUV is on average 56% smaller than coincident values from COSMIC-2. Based on the biases reported by Wautelet et al. (2021, 2022), a scale factor ~16-24 is not out of the realm of reasonability.
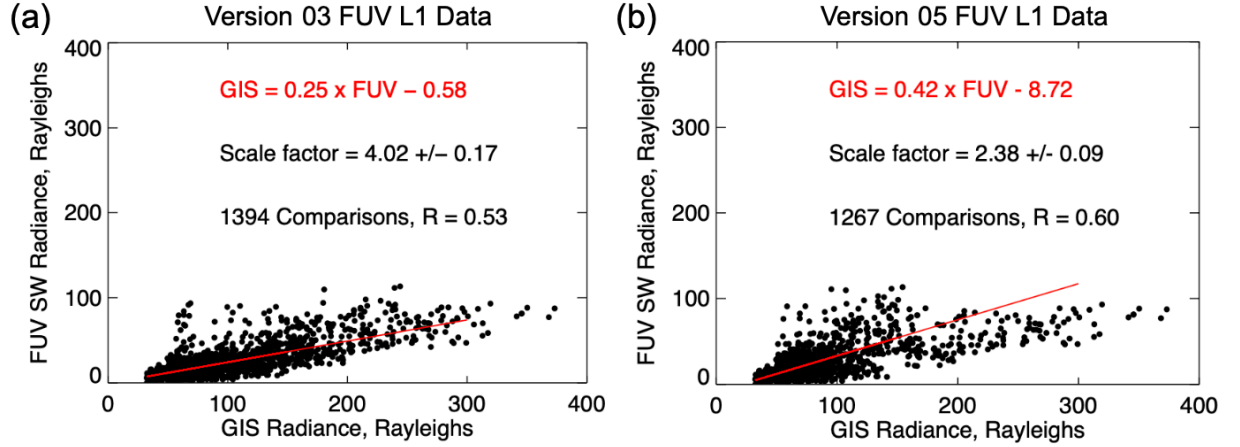
Figure 2. Comparison of observed nighttime radiance at 135.6 nm by the FUV instrument onboard the Ionospheric Connection Explorer to modeled radiance at 135.nm based on electron density maps from GIS. Comparisons are from days 73-94 of 2020 during conditions as specified by the text. Panel (a) uses Version 3 ICON-FUV L1 data which is the basis of the subsequent results. Panel (b) uses Version 5. Printed on the figure are the line of best fit, the GIS-to-FUV scale factor and its uncertainty, the number of comparisons, and the linear correlation coefficient of the observations and model results after the scale factor adjustment. The line of best fit is plotted in red.

The next step in reprocessing the FUV disk data is to run the operational ICON-FUV $\Sigma O/N_2$ algorithm with modified SW radiances from which the ionosphere contribution has been subtracted. This is done for each the three models of the ionospheric contribution: GIS, IRI, and EUV. Uncertainties in the ionospheric contributions are estimated using the standard deviation of the 5 closest points. To propagate the uncertainty in the ionospheric contribution into the retrieval of $\Sigma O/N_2$, these uncertainties are added in quadrature with the uncertainty in the unmodified SW radiances.

To identify non-migrating tides, we perform longitudinal wavenumber decomposition as a function of latitude and day (local time) during different seasons: March-April 2020 and August-September 2020. The decomposition was carried out for the original and modified datasets in order to quantify the effects of the ionospheric contamination. Data for each day are averaged into 5° latitude bins. At each latitude, data are fitted to a zonal mean and Fourier modes corresponding to wavenumbers 1-4 using Equation 2 where λ is longitude in radians and $A_0,\ A_1, ... A_8$ are the fitting coefficients.

$$A_0 + A_1 \cos\left(\frac{\lambda}{2\pi}\right) + A_2 \sin\left(\frac{\lambda}{2\pi}\right) + A_3 \cos\left(2\frac{\lambda}{2\pi}\right) + A_4 \sin\left(2\frac{\lambda}{2\pi}\right) + A_5 \cos\left(3\frac{\lambda}{2\pi}\right) + A_6 \sin\left(3\frac{\lambda}{2\pi}\right) + A_7 \cos\left(4\frac{\lambda}{2\pi}\right) + A_8 \sin\left(4\frac{\lambda}{2\pi}\right) \quad (2)$$

In Section 4 we discuss differences in the longitudinal wave structure seen between the original and GIS-, IRI-, and EUV-based modified datasets during the two time periods.

4) Results

Figure 3 presents histograms showing the occurrence rate of the ionospheric contribution to the total shortwave (SW) radiance during the two time periods examined: DOY 73-94 and DOY 218-241, both in 2020, and hereafter referred to as time period 1 and time period 2. These plots were produced using the modified dataset based on GIS electron density. Similar plots for the modified datasets based on either IRI or ICON-EUV exhibit similar trends and are thus not shown here but are in the supplementary information file (Figures S1 and S2). The data sampled for these histograms are at 20° latitude on the descending node of the ICON orbit (to match the dataset used in the analysis corresponding to Figure 4 that follows). The distribution is presented as the occurrence rate (percent of all data points satisfying the above criteria) of ionospheric contribution as a percent of the total SW radiance. On average, the DOY 73-94 time period (Figure 3a) has a higher ionospheric contribution than that during the DOY 218-241 time period (Figure 3b). It is noteworthy that this bias is also present in both the estimates based on IRI and ICON-EUV (Figures S1 and S2). This has implications on the expected differences seen between the original dataset and the modified dataset.

Solar and geomagnetic activity levels were explored as possible reasons for the difference between time periods 1 and 2. It was found that the respective F10.7 and Kp indexes were similar during each time period and thus solar or geomag-

netic activity variation does not explain why the ionospheric contribution to SW is higher during time period 1 than that during time period 2. The root cause of the difference is the higher average electron density present in GIS during time period 1 as compared to that during time period 2. Kil et al. (2013) found that in GUVI data during 2002 August 31 – September 2, the ionospheric contribution can be as large 10% around the equatorial ionization anomaly around 15:00 LT. Figure 3b indicates negligible occurrence rate for ionospheric contribution larger than 7% during 2020 at a similar time of year to the analysis of Kil et al. (2013). Although, it is worthwhile to note that 2002 experienced much higher solar activity than in 2020. Higher solar activity should produce a higher percentage of the ionospheric contribution to the total signal at 135.nm because (1) total electron content (TEC) increases by about a factor of 5 from solar minimum to maximum (Lean et al., 2011), and (2) the total dayglow at 135.6 nm increases by about a factor of 3 from solar minimum to maximum (Meier et al., 2015).

(a) 2020/73 - 2020/94

(b) 2020/218 - 2020/241
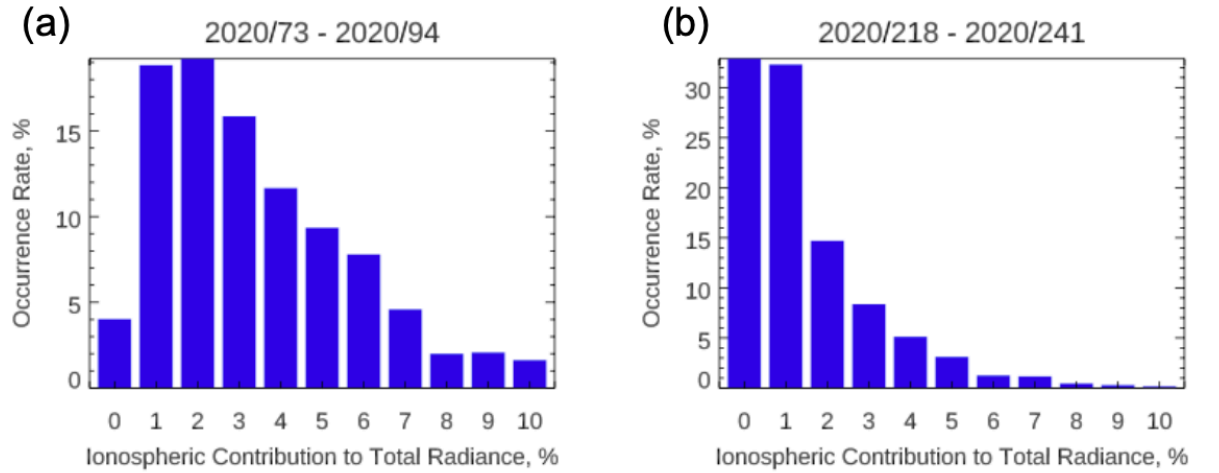
Figure 3. The distribution of ionospheric contribution to the total radiance at 135.6 nm observed by ICON-FUV during days 73-94 (a) and days 218-241(b) in 2020 based on the GIS dataset. Data are located between -17.5° and 22.5° latitude on the descending node of the ICON orbit.

Figure 4 provides a summary of the longitudinal–local time variation of $\Sigma O/N_2$ and the estimated ionospheric contribution to the SW radiance decomposed into a wavenumber-3 pattern during time period 1 and a wavenumber-4 pattern during time period 2. Data used during each time period were between 17.5° and 22.5° latitude on the descending node of the ICON orbit. There were low solar and geomagnetic conditions during both time periods. Each panel in Figure 4 shows the longitudinal wavenumber reconstruction as a function of longitude and day of year. As indicated by the upper horizontal axis, the orbital coverage

of local solar time is a function of day of year, decreasing with the precession of the ICON orbit. These plots are generated based on the amplitudes and phases computed by fitting for Fourier coefficients using Equation 2 as discussed in the previous section. The amplitudes and phases and their uncertainties are presented in the Supplementary Information file (refer to Figures S3, S4, S5, and S6). Figures 4a and 4b respectively show the wave-3 pattern during time period 1 in the original dataset and the modified dataset based on GIS. Figures 4d and 4e are the same as Figures 4a and 4b except for the wave-4 pattern in $\Sigma O/N_2$ during time period 2. Figures 4c and 4f respectively show the wave-3 and wave-4 pattern in the ionospheric contribution during time period 1 and time period 2.

It is evident that the wave-3 pattern changes after 12:00 LST in the original dataset during time period 1 (Figure 4a). For reference, the theoretical phase slopes of DE2 (120° longitude / 24 h) and SE1 (120° longitude / 12 h) are shown respectively as dashed and solid lines. The morphology in Figure 4a clearly does not match either slope. After correction for the ionospheric contamination, the wave-3 pattern in the GIS-modified dataset obviously tracks the phase slope of DE2 (Figure 4b). The ionospheric contribution to the SW radiance during the afternoon hours of Figure 4a has a strong eastward propagation seen in the wave-3 decomposition of Figure 4c, which masks the true tidal signal.

In contrast to period 1, during time period 2 there is negligible difference in wave-4 between the original dataset (Figure 4d) and the GIS-modified dataset (Figure 4e). The DE3 and SE2 theoretical phase slopes are shown to indicate to the reader that the local time progression resembles that expected for SE2 rather than DE3. Figure 4f indicates an approximately stationary pattern in the wave-4 decomposition of the ionospheric contribution to 135.6 nm during the afternoon hours. This stationary pattern seems to vanish at the beginning of time period 2. The cause of this difference between the two time periods can be best explained by Figure 3 which shows that on average the ionospheric contribution to the total SW radiance is lower during time period 2 than during time period 1. The correction for ionospheric contamination during time period 2 (Figure 4d) is sufficiently small that there is little change in the pattern (Figure 4e).
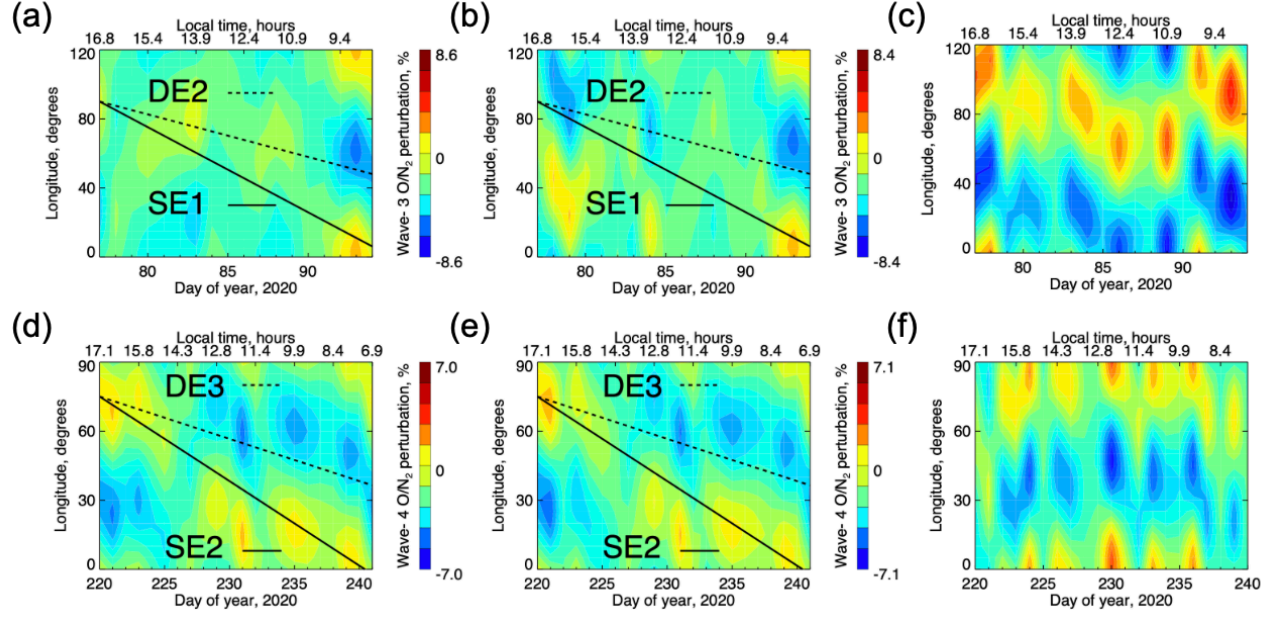
Figure 4. (a) Longitudinal wavenumber-3 reconstruction as a function of longitude and day of year (local time) in the original $\Sigma O/N_2$ dataset during a time period in March-April 2020 at 20° N on the descending node portion of the ICON orbit. Presented as percent deviation about the background zonal mean $\Sigma O/N_2$. The DE2 and SE1 phase slopes are shown for reference as dashed and solid lines respectively. (b) Same as (a) but for the modified $\Sigma O/N_2$ dataset based on GIS data. (c) Longitudinal wavenumber-3 reconstruction of the GIS-based estimated ionospheric contribution to the SW radiances used in the $\Sigma O/N_2$ retrieval. Units of percent relative to the zonal mean SW radiance. (d), (e), and (f) are the same as (a), (b), and (c) except for a time period in August-September 2020 and the DE3 and SE2 phase slopes are shown for reference.

5) Discussion of Results

In order to provide insight and understanding of the tidal signatures observed in Section 4, we introduce model expectations using TIEGCM-ICON and Hough Mode Extensions (Section 2.4). Figure 5 shows tidal amplitudes in $\Sigma O/N_2$ calculated from TIEGCM-ICON during time period 1 and time period 2 at 20° latitude. For time periods 1 and 2, wavenumber-3 and wavenumber-4 tides are shown respectively. The total wavenumber-3 perturbation caused by tides is a superposition of DE2 and SE1, along with a more minor contribution from DW4 and SW5. DE2 is the strongest or equal strongest wave-3 tide throughout the time period. Similarly, the total wavenumber-4 perturbation caused by tides is a superposition of DE3 and DW5, along with a more minor contribution from SE2 and SW6. DE3 is the dominant wave-4 tide during time period 2 except at the very beginning when DW5 is largest. The modeled amplitudes seem to

underestimate the total wavenumber-3 and wavenumber-4 amplitudes from the ICON analysis in Figure 4 but do match the dominant tide apparent in the observations. This tendency to underestimate the tidal amplitude in $\Sigma O/N_2$ is consistent with the earlier findings of England et al. (2021), who did not correct the ICON SW data for radiative recombination.
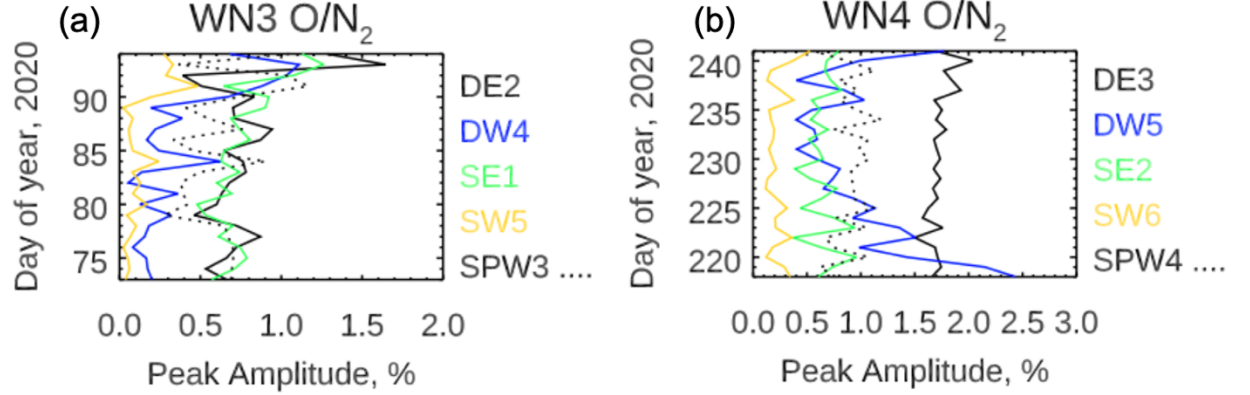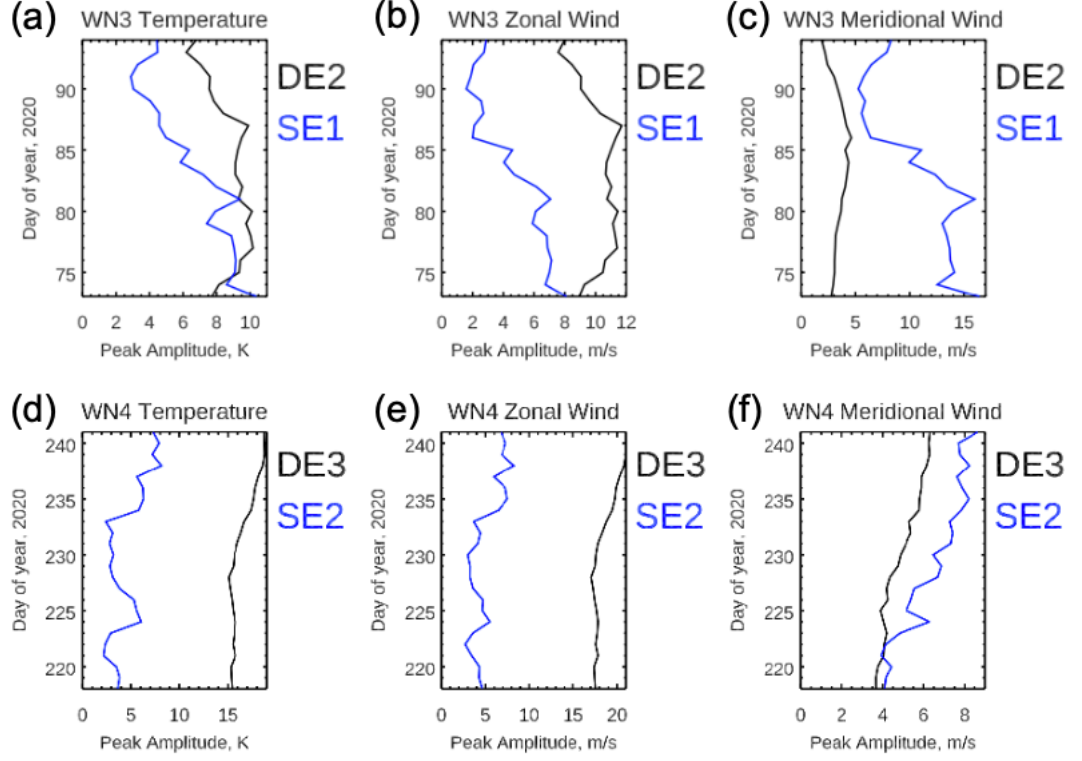

Figure 5. (a) Wavenumber-3 tidal amplitudes around 20° latitude as a function of day of year modeled by TIEGCM-ICON during a time period in March-April 2020. (b) Same as (a) except for wavenumber-4 during a time period in August-September 2020.

Figure 6 summarizes the relevant tides from HME-ICON output. These HME tides reflect only tides propagating from the lower atmosphere and do not include any that may be generated above ~105 km altitude. Tides for which ICON-HME specification is not available are not shown in Figure 6, i.e., DW4, SW5, DW5, SW6. Peak amplitudes (as a function of altitude) at 20° latitude in temperature and zonal/meridional winds are shown as a function of day during each time period. DE2 (DE3) are the strongest wavenumber-3 (4) tides in temperature and zonal wind throughout their respective time period which is consistent with their long vertical wavelengths. The presence of DE2 in the modified $\Sigma O/N_2$ (Figure 4b) dataset is consistent with both the HME output and the fact that DE2 has an exceptionally long vertical wavelength (Truskowski et al., 2014) allowing DE2 to be prominent in the vertically integrated $\Sigma O/N_2$. This suggests that the GIS-modified $\Sigma O/N_2$ dataset faithfully reflects the tidal dynamics in thermospheric composition during time period 1. The eastward trend seen in Figure 4d and 4e is consistent with the expectation that DE3 is the strongest wavenumber-4 tide (with SE2 also playing role) and this is confirmed by HME output during time period 2. The phase slope reflects SE2, which indicates that the wavenumber-4 origin is more complex than solely being caused by DE3. This is consistent with the conclusion of a case study of wavenumber-4 tides that employed physics-based empirical modeling and observations from the TIMED and CHAMP satellites (Oberheide et al., 2011). Note that the vertical wavelength of the most important Hough mode to SE2 is much longer

than that for DE3, making it not so surprising that SE2 can be more prominent in $\Sigma O/N_2$.

Figure 6. ICON Hough Mode Extension wavenumber-3 tide peak amplitudes around 20° latitude as a function of day of year in temperature (a), zonal wind (b) and meridional wind (c) during DOY 73-94. The respective wavenumber-4 amplitudes during DOY 218-241 are shown in (d), (e), and (f).

It is worthwhile to compare this work to previous findings based on TIMED/GUVI data. Kil et al. (2013) estimated the ionospheric contamination of $\Sigma O/N_2$ to be 5 – 10 % from 31 August to 2 September 2002, much larger than the typical values seen in Figure 4. Kil et al. (2013) proved that the longitudinal variation at a fixed local time were caused by ionospheric contamination of GUVI data during that time period. In contrast, the results in the previous section show that at least some of the time, the ionospheric contribution does not modulate the longitudinal variation in ICON-FUV data. The solar activity was much higher in 2002 than in 2020 which may partially explain the difference in results as the ionospheric contribution is expected to be greater at higher solar activity (see discussion in Section 4). On the other hand, Zhang et al. (2010) found that wave-3 and wave-4 peak to valley vary from 7-11 % in TIMED/GUVI data in 2009, a period of very low solar

activity. Such amplitudes are in better agreement with ICON-FUV (Figures S3 and S5 in the supporting information file) and thus also higher than the TIEGCM-ICON amplitudes.

6) Conclusions

Isolating and quantifying purely thermospheric tidal perturbations in $\Sigma O/N_2$ leads to a more complete description of tidal-ionosphere coupling. In this paper, we have presented a method that removes most of the ionospheric contamination of the retrieval of $\Sigma O/N_2$ from measurements by the FUV imager onboard the Ionospheric Connection Explorer. In doing so, we have presented the first investigation of the tidal longitudinal - local time evolution of $\Sigma O/N_2$ that is not compromised by ionospheric contamination effects. We assessed estimates of the ionospheric contribution based on either the GIS, IRI, or ICON-EUV datasets which are adjusted, based on the biases between the ionospheric specifications and the airglow. After removing the ionospheric signal from the SW data, we reran the ICON-FUV operational disk retrieval algorithm to provide corrected $\Sigma O/N_2$. In turn, we reexamine the longitudinal wavenumber-3 and wavenumber 4 structure during times from March-April 2020 and August-September 2020 respectively, noting differences between the original and modified $\Sigma O/N_2$ datasets. This work presents a framework for application to $\Sigma O/N_2$ datasets from other science missions and motivates further modeling/theoretical analyses. A list of conclusions from this study is as follows:

1. Scale factors for increasing the GIS/IRI/EUV based calculations of the ionospheric contribution to daytime 135.6 nm were calculated to properly reduce the ionospheric contamination in Version 3 ICON-FUV SW radiances. This accounts for differences between the various versions of the ICON-FUV Level 1 radiances. Such analyses should be performed on a version-by-version basis for each specification of electron density.

2. In the modified $\Sigma O/N_2$ dataset based on GIS ionospheric corrections, a DE2-like pattern is evident in the longitudinal wavenumber-3 variations during March-April 2020. HME-ICON tides and TIEGCM-ICON confirm that DE2 is present during that time. Ionospheric contamination of the original dataset masked the DE2-like pattern. This suggests that the GIS-based correction closely reflects the real atmosphere.

3. Observed amplitudes are higher than those modeled by TIEGCM-ICON in agreement with the earlier study by England et al. (2021).

4. No difference in the longitudinal wavenumber-4 structure is observed between the original and modified $\Sigma O/N_2$ during August-September 2020 because the ionospheric correction is much lower than in the earlier period. In contrast, Kil et al., (2013) showed that the ionospheric contamination dominated the retrieved tidal response seen in GUVI $\Sigma O/N_2$ during the same season in 2002. The most probable cause for this inconsistency is the much higher solar activity in 2002 than that in 2020. Future work will reproduce this analysis on ICON data collected during the anticipated solar maximum.

5. There is greater ionospheric contribution to the SW radiance during March-April 2020 than during August-September 2020, which causes the more pronounced change in the modified $\Sigma O/N_2$ in the former time period.

Data Availability Statement

Acknowledgements

References

Bilitza, D. (2001). International reference ionosphere 2000. *Radio Science*, 36(2), 261–275. https://doi.org/10.1029/2000rs002432

Chang, L. C., C.-H. Lin, J. Yue, J.-Y. Liu, and J.-T. Lin (2013), Stationary planetary wave and nonmigrating tidal signatures in ionospheric wave 3 and wave 4 variations in 2007–2011 FORMOSAT-3/COSMIC observations, *J. Geophys. Res. Space Physics*, *118*, 6651–6665, doi:10.1002/jgra.50583.

Christensen, A. B., et al (2003)., Initial observations with the Global Ultraviolet Imager (GUVI) in the NASA TIMED satellite mission, *J. Geophys. Res.*, 108(A12), 1451, doi:10.1029/2003JA009918.

Cui, J., R. V. Yelle, T. Li, D. S. Snowden, and I. C. F. Müller-Wodarg (2014), Density waves in Titan s upper atmosphere, *J. Geophys. Res. Space Physics*, *119*, 490–518, doi:10.1002/2013JA019113.

Cullens, C. Y., Immel, T. J., Triplett, C. C., Wu, Y.-J., England, S. L., Forbes, J. M., & Liu, G. (2020). Sensitivity study for ICON tidal analysis. *Progress in Earth and Planetary Science*, *7*, 18. https://doi.org/10.1186/s40645-020-00330-6

England, S. L. (2012), A review of the effects of non-migrating atmospheric tides on the Earth's low-latitude ionosphere, *Space Sci. Rev.*, *168*, 211–236, doi:10.1007/s112140119842-4.

England, S. L., Immel, T. J., Huba, D., Hagan, M. E., Maute, A., & DeMajistre, R. (2010). Modeling of multiple effects of atmospheric tides on the ionosphere: An examination of possible coupling mechanisms responsible for the longitudinal structure of the equatorial ionosphere. *Journal of Geophysical Research*, *115*, A05308. https://doi.org/10.1029/2009JA014894

England, S. L., Meier, R. R., Frey, H. U., Mende, S. B., Stephan, A. W., Krier, C. S., et al. (2021). First results from the retrieved column O/N_2 ratio from the Ionospheric Connection Explorer (ICON): Evidence of the impacts of nonmigrating tides. *Journal of Geophysical Research: Space Physics*, *126*, e2021JA029575. https://doi.org/10.1029/2021JA029575

Evans, J. S., Strickland, D. J., Huffman, R. E., & Eastes, R. W. (1995). Satellite remote sensing of thermospheric O/N_2 and solar EUV, 2. Data analysis. *Journal of Geophysical Research*, 100(A7), 12217–12226. https://doi.org/10.1029/95JA00573

Forbes, J. M., Russell, J., Miyahara, S., Zhang, X., Palo, S., Mlynczak, M., et al. (2006). Troposphere-thermosphere tidal coupling as measured by the SABER instrument on TIMED during July–September 2002. *Journal of Geophysical Research*, *111*, A10S06. https://doi.org/10.1029/2005JA011492

Forbes, J. M., Zhang, X., Hagan, M. E., England, S. L., Liu, G., & Gasperini, F. (2017). On the specification of upward-propagating tides for ICON science investigations. *Space Science Reviews*, *212*, 697–713. https://doi.org/10.1007/s11214-017-0401-5

Forbes, J. M., Zhang, X., Palo, S., Russell, J., Mertens, C. J., & Mlynczak, M. (2008). Tidal variability in the ionospheric dynamo region. *Journal of Geophysical Research*, *113*, A02310. https://doi.org/10.1029/2007JA012737

Frey et al. (2022). In flight performance of the Far Ultraviolet Instrument (FUV) on ICON, Submitted to *Space Science Reviews*, SPAC-S-22-00058.

Goncharenko, L. P., Chau, J. L., Liu, H.-L., & Coster, A. J. (2010). Unexpected connections between the stratosphere and ionosphere. *Geophysical Research Letters*, *37*, L10101. https://doi.org/10.1029/2010GL043125

Hagan, M. E., & Forbes, J. M. (2002). Migrating and nonmigrating diurnal tides in the middle and upper atmosphere excited by tropospheric latent heat release. *Journal of Geophysical Research*, *107*(D24), 4754. https://doi.org/10.1029/2001JD001236

Harding, B. J., Makela, J. J., Englert, C. R., Marr, K. D., Harlander, J. M., England, S. L., & Immel, T. J. (2017). The MIGHTI wind retrieval algorithm: Description and verification. *Space Science Reviews*, 212, 585–600. https://doi.org/10.1007/s11214-017-0359-3

He, M., L. Liu, W. Wan, J. Lei, and B. Zhao (2010), Longitudinal modulation of the O/N_2 column density retrieved from TIMED/GUVI measurement, *Geophys. Res. Lett.*, 37, L20108, doi:10.1029/2010GL045105.

Immel, T. J., England, S. L., Mende, S. B., et al. (2018). The ionospheric connection explorer mission: Mission goals and design. *Space Science Reviews*, 214, 13. https://doi.org/10.1007/s11214-017-0449-2

Immel, T. J., E. Sagawa, S. L. England, S. B. Henderson, M. E. Hagan, S.

B. Mende, H. U. Frey, C. M. Swenson, and L. J. Paxton (2006), Control of equatorial ionospheric morphology by atmospheric tides, *Geophys. Res. Lett.*, 33, L15108, doi:10.1029/2006GL026161.

Jones, M., Jr., J. M. Forbes, and M. E. Hagan (2014), Tidal-induced net transport effects on the oxygen distribution in the thermosphere, *Geophys. Res. Lett.*, *41,* 5272–5279, doi:10.1002/2014GL060698.

Kamalabadi, F., Qin, J., Harding, B. J., Iliou, D., Makela, J. J., Meier, R. R., et al. (2018). Inferring nighttime ionospheric parameters with the far ultraviolet imager onboard the ionospheric connection explorer. *Space Science Reviews*, 214(4), 70. https://doi.org/10.1007/s11214-018-0502-9

Kil, H., W. K. Lee, J. Shim, L. J. Paxton, and Y. Zhang (2013), The effect of the 135.6 nm emission originated from the ionosphere on the TIMED/GUVI O/N_2 ratio, *J. Geophys. Res. Space Physics*, *118*, 859–865, doi:10.1029/2012JA018112.

Kil, H., and L. J. Paxton (2011), The origin of the nonmigrating tidal structure in the column number density ratio of atomic oxygen to molecular nitrogen, *Geophys. Res. Lett.*, 38, L19108, doi:10.1029/2011GL049432.

Krier, C. S., England, S. L., Greer, K. R., Evans, J. S., Burns, A. G., & Eastes, R. W. (2021). Deducing non-migrating diurnal tides in the middle thermosphere with GOLD observations of the Earth's far ultraviolet dayglow from geostationary orbit. *Journal of Geophysical Research: Space Physics*, *126*, e2021JA029563. https://doi.org/10.1029/2021JA029563

Lean, J. L., R. R. Meier, J. M. Picone, and J. T. Emmert (2011), Ionospheric total electron content: Global and hemispheric climatology, J. Geophys. Res., 116, A10318, doi:10.1029/2011JA016567

Lieberman, R. S., Oberheide, J., & Talaat, E. R. (2013). Nonmigrating diurnal tides observed in global thermospheric winds. *Journal of Geophysical Research: Space Physics*, *118*, 7384–7397. https://doi.org/10.1002/2013JA018975

Lin, C. Y., Lin, C. C., Liu, J., Rajesh, P. K., Matsuo, T., Chou, M., et al. (2020a). The Early Results and Validation of FORMOSAT-7/COSMIC-2 Space Weather Products: Global Ionospheric Specification and Ne-Aided Abel Electron Density Profile. *Journal of Geophysical Research: Space Physics*, 125(10), 1–12. https://doi.org/10.1029/2020JA028028

Lin, C. Y., Matsuo, T., Liu, J. Y., Lin, C. H., Huba, J. D., Tsai, H. F., & Chen, C. Y. (2017). Data assimilation of ground-based GPS and radio occultation total electron content for global ionospheric specification. *Journal of Geophysical Research: Space Physics*, 122(10), 10876–10886. https://doi.org/10.1002/2017JA024185

Lin, J. T., Lin, C. H., Rajesh, P. K., Yue, J., Lin, C. Y., & Matsuo, T. (2020b). Local-time and vertical characteristics of quasi-6-day oscillation in the iono-

sphere during the 2019 Antarctic Sudden stratospheric warming. *Geophysical Research Letters*, 47(21). https://doi.org/10.1029/2020GL090345

Liu, L., W. Wan, B. Ning, O. M. Pirog, and V. I. Kurkin (2006), Solar activity variations of the ionospheric peak electron density, *J. Geophys. Res.*, *111*, A08304, doi:10.1029/2006JA011598.

Maute, A. (2017). Thermosphere-ionosphere-electrodynamics general circulation model for the ionospheric connection explorer: TIEGCM-ICON. *Space Science Reviews*, 212(1-2), 523–551. https://doi.org/10.1007/s11214-017-0330-3.

Mende, S. B., Frey, H. U., Rider, K., Chou, C., Harris, S. E., Siegmund, O. H. W., et al. (2017). The far ultra-violet imager on the ICON mission. *Space Science Reviews*, *212*, 655–696. https://doi.org/10.1007/s11214-017-0386-0

Meier, R. R. (2021). The thermospheric column O/N$_2$ ratio. *Journal of Geophysical Research: Space Physics*, *126*, e2020JA029059. https://doi.org/10.1029/2020JA029059

Meier, R. R. (1991). Ultraviolet spectroscopy and remote sensing of the upper atmosphere, *Space Science Review, 58*, 1–186. https://doi.org/10.1007/BF01206000

Meier, R. R., Picone, J. M., Drob, D., Bishop, J., Emmert, J. T., Lean, J. L., et al. (2015). Remote sensing of Earth's limb by TIMED/GUVI: Retrieval of thermospheric composition and temperature. *Earth and Space Science*, 2, 1–37. https://doi.org/10.1002/2014EA000035

Meléndez-Alvira, D. J., R. R. Meier, J. M. Picone, P. D. Feldman, and B. M. McLaughlin (1999), Analysis of the oxygen nightglow measured by the Hopkins Ultraviolet Telescope: Implications for ionospheric partial radiative recombination rate coefficients, *J. Geophys. Res.*, *104*, 14,901–14,914. https://doi.org/10.1029/1999JA900136

Oberheide, J. (2022). Day-to-day variability of the semidiurnal tide in the F-region ionosphere during the January 2021 SSW from COSMIC-2 and ICON. *Geophysical Research Letters*, *49*, e2022GL100369. https://doi.org/10.1029/2022GL100369

Oberheide, J., J. M. Forbes, X. Zhang, and S. L. Bruinsma (2011), Wave-driven variability in the ionosphere- thermosphere-mesosphere system from TIMED observations: What contributes to the "wave 4"?, *J. Geophys. Res.*, *116*, A01306, doi:10.1029/2010JA015911.

Oberheide, J., Mlynczak, M. G., Mosso, C. N., Schroeder, B. M., Funke, B., & Maute, A. (2013). Impact of tropospheric tides on the nitric ox- ide 5.3 m infrared cooling of the low-latitude thermosphere during solar minimum conditions. *Journal of Geophysical Research: Space Physics*, *118*, 7283–7293. https://doi.org/10.1002/2013JA019278

Pedatella, N. M., Forbes, J. M., Maute, A., Richmond, A. D., Fang, T.-W., Larson, K. M., & Millward, G. (2011). Longitudinal variations in the F region ionosphere and the topside ionosphere-plasmasphere: Observations

and model simulations. *Journal of Geophysical Research*, *116*, A12309. https://doi.org/10.1029/2011JA016600

Picone, J. M., A. E. Hedin, D. P. Drob, and A. C. Aikin (2002), NRLMSISE-00 empirical model of the atmosphere: Statistical comparisons and scientific issues, *J. Geophys. Res.*, 107(A12), 1468, doi:10.1029/2002JA009430.

Roble, R. G., and G. G. Shepherd (1997), An analysis of wind imaging interferometer observations of O(^{1}S) equatorial emission rates using the thermosphere-ionosphere-mesosphere-electrodynamics general circulation model, *Journal of Geophysical Research*, *102,* 2467–2474, https://doi:10.1029/96JA02930

Sagawa, E., Immel, T. J., Frey, H. U., & Mende, S. B. (2005). Longitudinal structure of the equatorial anomaly in the nighttime ionosphere observed by IMAGE/FUV. *Journal of Geophysical Research*, *110*, 11302. https://doi.org/10.1029/2004JA010848

Sirk, M. M., Korpela, E. J., Ishikawa, Y., Edelstein, J., Wishnow, E. H., Smith, C., et al. (2017). Design and performance of the ICON EUV spectrograph. *Space Science Reviews*, *212*(1–2), 631–643. https://doi.org/10.1007/s11214-017-0384-2

Stephan, A. W., Korpela, E. J., Sirk, M. M., England, S. L., & Immel, T. J. (2017). Daytime ionosphere retrieval algorithm for the Ionospheric Connection Explorer (ICON). *Space Science Reviews*, 212(1–2), 645–654. https://doi.org/10.1007/s11214-017-0385-1

Stephan, A. W., Meier, R. R., England, S. L., Mende, S. B., Frey, H. U., & Immel, T. J. (2018). Daytime O/N_2 retrieval algorithm for the ionospheric connection explorer (ICON). *Space Science Reviews*, *214,* 42. https://doi.org/10.1007/s11214-018-0477-6

Stevens, M. H., Englert, C. R., Harlander, J. M., England, S. L., Marr, K. D., Brown, C. M., & Immel, T. J. (2018). Retrieval of lower thermo- spheric temperatures from O2 a band emission the MIGHTI experiment on ICON, *Space Science Reviews*, *214*, 4. https://doi.org/10.1007/s11214-017-0434-9

Strickland, D. J., Evans, J. S., & Paxton, L. J. (1995). Satellite remote sensing of thermospheric O/N_2 and solar EUV, 1. Theory. *Journal of Geophysical Research*, *100*(12), 217. https://doi.org/10.1029/95JA00574

Truskowski, A. O., Forbes, J. M., Zhang, X., & Palo, S. E. (2014). New perspectives on thermosphere tides - 1. Lower thermosphere spectra and seasonal-latitudinal structures. *Earth Planets and Space*, *66*, 136. https://doi.org/10.1186/s40623-014-0136-4

Wang, J. C., Palo, S. E., Forbes, J. M., Marino, J., Moffat-Griffin, T., & Mitchell, N. J. (2021). Unusual quasi 10-day planetary wave activity and the ionospheric response during the 2019 Southern Hemisphere sudden stratospheric warming. *Journal of Geophysical Research: Space Physics*, *126*, e2021JA029286. https://doi.org/10.1029/2021JA029286

Wautelet, G., Hubert, B., Gérard, J.-C., Immel, T. J., Frey, H. U., Mende, S. B., et al. (2021). First ICON-FUV nighttime NmF2 and hmF2 comparison to ground and space-based measurements. *Journal of Geophysical Research: Space Physics*, *126*, e2021JA029360. https://doi.org/10.1029/2021JA029360

Wautelet et al. (2022). Comparison of ICON-EUV O+ density profiles with external data sources. Submitted to *Space Science Reviews*.

Zhang, Y., S. England, and L. J. Paxton (2010), Thermospheric composition variations due to nonmigrating tides and their effect on ionosphere, *Geophys. Res. Lett.*, *37*, L17103, doi:10.1029/2010GL044313.

Zhang, Y., Paxton, L. J., & Schaefer, R. (2021). Ionospheric and thermospheric contributions in TIMED/GUVI O 135.6 nm radiances. *Journal of Geophysical Research: Space Physics*, *126*, e2021JA029333. https://doi.org/10.1029/2021JA029333